

# Comparison of a Neutral Density Model With the SET HASDM Density Database

Daniel R. Weimer<sup>1,2</sup>, W. Kent Tobiska<sup>3</sup>, Piyush M. Mehta<sup>4</sup>, R. J. Licata<sup>4</sup>,  
Douglas P. Drob<sup>5</sup>, Jean Yoshii<sup>3</sup>

<sup>1</sup>Center for Space Science and Engineering Research, Virginia Tech, Blacksburg, Virginia, USA

<sup>2</sup>National Institute of Aerospace, Hampton, Virginia, USA

<sup>3</sup>Space Environment Technologies, Los Angeles, California, USA

<sup>4</sup>Department of Mechanical and Aerospace Engineering, Statler College of Engineering and Mineral  
Resources, West Virginia University, Morgantown, WV, USA

<sup>5</sup>Space Science Division, U.S. Naval Research Laboratory, Washington, District of Columbia, USA

## Key Points:

- Thermosphere neutral densities from the EXEMPLAR model are compared with the SET HASDM density database for a 20 year time period
- The use of mean densities on spherical shells at several altitudes is an effective way to compare the models
- The EXEMPLAR model performs well at altitudes of 400 km and above where geomagnetic storms produce the largest changes in neutral density

**Abstract**

The EXospheric TEMperatures on a PoLyhedrAl gRid (EXTEMPALAR) method predicts the neutral densities in the thermosphere. The performance of this model has been evaluated through a comparison with the Air Force High Accuracy Satellite Drag Model (HASDM). The Space Environment Technologies (SET) HASDM database that was used for this test spans the 20 years 2000 through 2019, containing densities at 3 hour time intervals at 25 km altitude steps, and a spatial resolution of 10 degrees latitude by 15 degrees longitude. The upgraded EXTEMPALAR that was tested uses the newer Naval Research Laboratory MSIS 2.0 model to convert global exospheric temperature values to neutral density as a function of altitude. The revision also incorporated time delays that varied as a function of location, between the total Poynting flux in the polar regions and the exospheric temperature response. The density values from both models were integrated on spherical shells at altitudes ranging from 200 to 800 km. These sums were compared as a function of time. The results show an excellent agreement at temporal scales ranging from hours to years. The EXTEMPALAR model performs best at altitudes of 400 km and above, where geomagnetic storms produce the largest relative changes in neutral density. In addition to providing an effective method to compare models that have very different spatial resolutions, the use of density totals at various altitudes presents a useful illustration of how the thermosphere behaves at different altitudes, on time scales ranging from hours to complete solar cycles.

**Plain Language Summary**

A recently developed computer model predicts the mass density of atoms and molecules in upper atmosphere, in the region known as the thermosphere. Changes in this “neutral density” following geomagnetic storms can perturb the orbits of the many satellites in this region, leading to imprecise knowledge of their paths and risk of collisions. This model uses measurements of the solar wind and the embedded magnetic field to predict the level of heating in the upper atmosphere, and the resulting expansion of the atmosphere to higher altitudes. In order to test the capabilities of the new model, its calculations were compared with density values derived by an Air Force data assimilation system based on radar tracking of multiple objects in Earth orbit over a 20-year period. The results of this comparison show an excellent agreement, particularly at the higher altitudes where geomagnetic storms have the greatest influence.

## 1 Introduction

A major focus of space weather research has been on the topic of the mass density of the neutral atoms and molecules in the thermosphere. As the variations in this density perturb the orbital motion of satellites, there has been considerable effort in being able to predict these variations using both empirical models and numerical simulations (Bruinsma et al., 2018; J. Emmert, 2015).

Recently Weimer et al. (2020) had described a new empirical model that calculated exospheric temperatures, the asymptotic limit that the temperature in the thermosphere reaches at high altitudes (Prölss & Bird, 2004), often abbreviated as either  $T_{ex}$  or  $T_{\infty}$ . The temperature inputs to the model were derived from neutral density measurements from multiple satellites. Data from the Challenging Mini-satellite Payload (CHAMP) (Reigber et al., 2002; Bruinsma et al., 2004) in the years 2002 through 2009 were used, along with the Gravity Recovery and Climate Experiment (GRACE) satellites (Tapley et al., 2004), from 2003 through 2010. These total mass densities were derived from accelerometer measurements of the orbital drag. In our work we use density data from the CHAMP and GRACE missions provided by Mehta et al. (2017), who had recalibrated the drag coefficients and provided updated values of the neutral densities. The original data were from Sutton (2008). Additional density data were from the European Space Agency’s Swarm mission (Friis-Christensen et al., 2006), for the time period from 30 Nov 2013 through 2017. Orbital motions obtained from Global Positioning System (GPS) receivers on these spacecraft were used to determine the drag (Astafyeva et al., 2017; van den IJssel et al., 2020).

To create the empirical model, the temperature values were sorted into 1620 cells on a geodesic, polyhedral grid. These triangular grid cells have nearly equal areas and their edges have arc lengths of approximately  $7^{\circ}$ . Multiple linear regression fits were then used to obtain an equation for the exospheric temperature at each cell’s specific location, as a function of the input parameters. For convenience, the unique acronym EX-TEMPLAR was given to this method, for EXospheric TEMperatures on a PoLyhedral gRid. The Naval Research Laboratory Mass Spectrometer and Incoherent Scatter radar Extended (NRLMSISE-00) thermosphere model (Hedin, 1991; Picone et al., 2002) was originally used to convert the density measurements into the exospheric temperatures values that were used for the model development. (For this paper we use the newer, NRLM-

82 SIS 2.0 model (J. T. Emmert et al., 2020.) Afterwards the "MSIS" model (as commonly  
83 known) was used to calculate neutral densities using the exospheric temperatures out-  
84 put from EXTEMLAR for given locations and input parameters. Comparing such den-  
85 sity predictions with the original satellite measurements revealed a very good performance  
86 by the combination of the EXTEMLAR and MSIS models (hereafter referred to as sim-  
87 ply EXTEMLAR, with the MSIS component assumed). As there were on the order of  
88  $\approx 100,000$  data points in each grid cell, the regression formulas that used only six input  
89 variable and 16 coefficients could not contain a memory of specific time periods or events,  
90 so this was considered a valid test of the model. Nevertheless, a validation trial using  
91 an independent dataset is valuable.

92 The Air Force High Accuracy Satellite Drag Model (HASDM) (Storz et al., 2005)  
93 assimilates radar tracking of several dozens of calibration satellites to obtain thermospheric  
94 neutral densities. HASDM continuously adjusts coefficients in a modified Jacchia-Bowman  
95 2008 (JB2008) model (Bowman et al., 2008; Tobiska et al., 2008) to match the radar mea-  
96 surements. While the Combined Space Operations Center (CSpOC) of the United States  
97 Space Force (USSF) (previously part the Air Force) archives the temperature-correction  
98 coefficients that have been applied to the JB2008 atmosphere, these data are not avail-  
99 able to the public. Space Environment Technologies (SET) validates the HASDM out-  
100 puts under contract and produces a recreation of the densities of the global atmosphere,  
101 calling it the "SET HASDM density database" (Tobiska et al., 2021). With approval of  
102 the USSF, SET has released the density values for scientific use. These data span two  
103 solar cycles, from January 1, 2000 through December 31, 2019. As stated by Tobiska et  
104 al. (2021), "all solar cycle, geomagnetic storm and sub-storm, extended solar flare, and  
105 thermospheric cooling perturbations are embedded in the data. Because of its accuracy,  
106 time resolution, global scale, and information content, the SET HASDM database den-  
107 sities are suitable for use as a new space weather benchmark for atmospheric expansion  
108 against which space weather events are measured." The purpose of this paper is to present  
109 the results of a comparison between the EXTEMLAR and HASDM density values. The  
110 comparison was run for the entire, 20-year time period with a newer version of the EX-  
111 TEMPLAR model described in Section 3. In addition to serving as a useful validation  
112 tool, the results have provided helpful insights into the behavior of the thermosphere over  
113 the two solar cycles.

## 2 Density Calculations Using NRLMSIS

It is helpful to review how the MSIS model is used with the EXEMPLAR program in order to obtain the neutral densities. This description helps with understanding some of the results that will be shown. The standard input parameters for MSIS are the geographic coordinates, altitude, date, time, solar  $F_{10.7}$  index (both daily and 81-day average), and the daily  $A_p$  index of geomagnetic activity. There is an option to include values of the  $a_p$  index over six, 3-hour intervals. To obtain the neutral densities in the thermosphere, NRLMSIS 2.0 calculates the density of each atomic and molecular species at a boundary at 122.5 km altitude, along with the temperature and temperature gradient. Normally, MSIS also calculates the exospheric temperature for the given conditions and coordinates. The boundary conditions and exospheric temperature are then used to compute the density of each species as a function of altitude, as illustrated in the example in Figure 1. The species densities are summed to obtain the total density (the black line in the figure).

One shortcoming to the MSIS model is that the actual values of the  $A_p$  index are obtained only after measurements from magnetometers at selected, global locations are processed. So real-time indices are not available. While there are predictions of  $A_p$  available, they are only estimates. As geomagnetic indices are only an indirect proxy for the amount of heating that occurs in the polar regions, it is assumed that a model of the Poynting flux should be more accurate, as this energy flux has a more direct, physics-based relationship with the temperature changes. Furthermore, as the solar wind velocity and IMF values are the primary input needed to obtain the Poynting flux, values can be obtained from real-time measurements having an approximately 1 hr lead time, rather than much later. This lead time results from the time it takes the solar wind and IMF to travel from a satellite monitor located at an “upstream” position (Case & Wild, 2012) while the measurement data that are transmitted arrive much sooner. The physical relationship between the energy flux and temperatures plus the lead time are two reasons why the use of exospheric temperatures from the EXEMPLAR model is advantageous. It also uses the solar indices  $S_{10}$  and  $M_{10}$ , that are considered to be more accurate than  $F_{10.7}$  alone since they represent the actual solar irradiance being deposited into the thermosphere (Bowman et al., 2008; Tobiska et al., 2008).

145 With a small modification to the MSIS program, the exospheric temperature that  
146 is calculated by the EXEMPLAR model is included as a new input parameter. This  
147 temperature (if included in the input parameters) replaces the value that MSIS calcu-  
148 lates internally. Figure 2 illustrates the effect of changing the exospheric temperature  
149 in MSIS, with densities as a function of altitude shown for temperatures of 600, 1000,  
150 1400, 1800, and 2200°K. Note that at an altitude of 200 km, the exospheric tempera-  
151 ture variations have little effect on the modeled density.

### 152 **3 Recent EXEMPLAR Modifications**

153 Work is presently under way to improve the EXEMPLAR method and develop  
154 a real-time, operational program, so the version used in this comparison is similar to but  
155 not exactly identical to what was described by Weimer et al. (2020). One difference is  
156 that the we now use the newer NRLMSIS 2.0 model (J. T. Emmert et al., 2020) rather  
157 than NRLMSISE-00. This change will enable use of future updates to this model, but  
158 it also resulted in a need to recalculate all temperature values used in the EXEMPLAR  
159 model development, the reason being that the newer version of the MSIS model produces  
160 densities lower than the original version for the same input conditions.

161 An exospheric temperature is derived from a density with use of the MSIS model  
162 by means of a reiterative substitution of revised exospheric temperatures in the model  
163 until the model’s output density at the given coordinates matches the measured value.  
164 The bisection method is used, with the search terminating when the resolution is within  
165 2°K. The result is called the measured temperature. The process is repeated for every  
166 density measurement in the database.

167 For this method to work, the density measurements need to match, on average, the  
168 unmodified MSIS model as much as possible during or else the derived temperature val-  
169 ues may be excessively high or low. The density measurements from the various satel-  
170 lites may need to be multiplied by a correction factor in order to produce the best over-  
171 all match with the densities from the MSIS model. The process is described by Weimer  
172 et al. (2016) using the original CHAMP and GRACE data (Sutton, 2008). Later Weimer  
173 et al. (2018) had derived different correction factors for the newer, higher-resolution den-  
174 sity values provided by Mehta et al. (2017) for these satellites, and these same factors  
175 were used for the original EXEMPLAR model Weimer et al. (2020). For example, the

176 CHAMP data were all multiplied by a factor of 1.12 before calculating the temperatures.  
177 The new NRLMSIS 2.0 model actually matched the CHAMP densities very well with-  
178 out any adjustment, so the correction factor was changed to 1. The correction factor for  
179 the GRACE A satellite varies over time from 1. to 1.2, depending on the date, while a  
180 factor of 1.08 was used for densities from all Swarm satellites.

181 The previous work by Weimer et al. (2020) originally had an objective to deter-  
182 mine whether or not satellite measurements of emissions from nitric oxide could be used  
183 in predictions of thermospheric temperatures and density. Several versions of the EX-  
184 TEMPLAR formula were reported, with Versions 1 through 5 using the measured ni-  
185 tric oxide emissions in the temperature calculation. The sixth version used a simulated  
186 value of the extra cooling due to nitric oxide within a difference equation (details below)  
187 rather than measured values. As nitric oxide emission measurements are not presently  
188 available in real time, the most recent EXTEMPLAR model is most closely related to  
189 the previous Version 6, that used only solar indices and Poynting flux values from an em-  
190 pirical model (Weimer, 2005a, 2005b) that can use historical or real-time solar wind and  
191 Interplanetary Magnetic Field (IMF) measurements.

192 The EXTEMPLAR model that was used in this comparison with the HASDM data  
193 is referred to as Version 2.4.2, since is a second-generation model, using the fourth (of  
194 several) iterations that were tested, and using version 2 of the NRLMSIS model. As be-  
195 fore, the exospheric temperatures are calculated separately for each of 1620 grid cells;  
196 this grid is obtained from a 20-facet icosahedron, in which each facet is subdivided into  
197 81 equilateral triangles, with the new vertices projected outward to a sphere. A new fea-  
198 ture is that the Poynting flux values are delayed in time, with different time delays used  
199 for each grid cell. The result is that when the auroral heating suddenly increases the tem-  
200 peratures in the grid cells near the pole will increase sooner than at locations near the  
201 equator, that have a delayed response. Details about these delays will be reported in a  
202 separate publication.

203 The exospheric temperature in each grid cell is obtained from this formula:

$$\begin{aligned}
 T_{\infty N} = & C_0 + C_1 S_{10} + C_2 S_{10} \sin(\theta_D) + C_3 S_{10} \cos(\theta_D) + \\
 & C_4 \sqrt{M_{10}} + C_5 \sqrt{M_{10}} \sin(\theta_D) + C_6 \sqrt{M_{10}} \cos(\theta_D) + \\
 & C_7 \sin(2\theta_D) + C_8 \cos(2\theta_D) + C_9 \sin(\phi_{UT}) + C_{10} \cos(\phi_{UT}) + \\
 & C_{11} S_T(\delta t_N) \sin(\phi_{UT}) + C_{12} S_T(\delta t_N) \cos(\phi_{UT}) + C_{13} S_T(\delta t_N) + \\
 & C_{14} \Delta T \sin(\theta_D) + C_{15} \Delta T \cos(\theta_D) + C_{16} \Delta T
 \end{aligned} \tag{1}$$

205  $T_{\infty N}$  is the exospheric temperature in cell number  $N$ .  $S_{10}$  and  $M_{10}$  are solar proxy in-  
 206 dices that were developed for use in the JB2008 density model (Tobiska et al., 2008; Thayer  
 207 et al., 2021). Predictions of these indices are produced by SET, with updated values pro-  
 208 vided in near real-time. The recent and historical  $S_{10}$  and  $M_{10}$  solar indices are freely avail-  
 209 able at the JB2008 website <https://spacewx.com/jb2008/> while the predicted values  
 210 are publicly, commercially available through the US Space Force Unified Data Library.  
 211  $\theta_D$  is calculated using  $2\pi DOY/365.25$ , which is the Day-Of-Year date converted to ra-  
 212 dians, and  $\phi_{UT} = 2\pi UT/24$  is the Universal Time (UT) converted to radians. The  $C_7$   
 213 and  $C_8$  terms reproduce semi-annual/inter-annual variations in the data.  $S_T(\delta t_N)$  rep-  
 214 represents Poynting flux values that have been delayed in time by an amount that is unique  
 215 for each grid cell  $N$ . Sums of the Poynting flux are actually calculated for both the North-  
 216 ern and Southern Hemispheres. As described by Weimer et al. (2020), these totals are  
 217 combined with a formula that varies smoothly from one hemisphere to the other:

$$S_T = S_N \sin^2(0.5 * (Latitude + \pi/2)) + S_S \sin^2(0.5 * (Latitude - \pi/2)) \tag{2}$$

219 where  $S_N$  and  $S_S$  are the total Poynting flux values in the Northern and Southern hemi-  
 220 spheres respectively. The latitude is determined from the coordinates of each grid cell's  
 221 geometric center. In radians, this latitude ranges from  $-\pi/2$  to  $+\pi/2$ . The Poynting flux  
 222 values in this version are smoothed with a boxcar averaging function having a width of  
 223 1 hr, prior to the application of the time delays, that range from 39 min in polar regions  
 224 to 6.6 hr at low latitudes.

225 The  $\Delta T$  in (1) represent a global perturbation to the exospheric temperature, that  
 226 varies in each grid cell in proportion to  $C_{14}$ ,  $C_{15}$ , and  $C_{16}$ .  $\Delta T$  varies in time, as calcu-  
 227 lated with the following numerical difference equation:

$$\Delta T(t_{n+1}) = \Delta T(t_n) - \Delta T(t_n) \left( \frac{\delta t}{\tau_c} \right) + \alpha S_T(t_n) - P_{NO}(t_n) \tag{3}$$

229 In each time step  $\Delta T$  increases in proportion ( $\alpha$ ) to the total Poynting flux in both hemi-  
 230 spheres ( $S_T$ ), and decays at an exponential rate with time constant  $\tau_c$ .  $\Delta T$  is further

231 decreased by  $P_{NO}$ , which represents the cooling due to nitric oxide emissions. This sim-  
 232 ulated cooling is calculated with difference equations, using exactly the same methods  
 233 described by Weimer et al. (2020) in their equations (10) and (11), rather than using mea-  
 234 sured emissions. As in the previous versions of the model, the various parameters in the  
 235 difference equations were optimized through reiterative fits of the  $T_{\infty N}$  from (1) with all  
 236 temperature values in each cell.

#### 237 4 Comparison with HASDM

238 The complete SET HASDM density database is available at [https://spacewx.com/](https://spacewx.com/hasdm/)  
 239 [hasdm/](https://spacewx.com/hasdm/). As indicated by Tobiska et al. (2021), this data “covers the period from Jan-  
 240 uary 1, 2000 through December 31, 2019. Data records exist every 3 h during solar cy-  
 241 cles 23 and 24. The database has a grid size of  $10^\circ \times 15^\circ$  (latitude, longitude) with 25  
 242 km altitude steps between 175 and 825 km.” One difficulty is that the resolution of this  
 243 grid is much more coarse than that used in the EXEMPLAR model, in which the tri-  
 244 angular cells have edge lengths of approximately  $7^\circ$ , and their centers are separated by  
 245 as little as  $4.3^\circ$  between adjacent triangles. As the HASDM model, and the JB2008 model  
 246 from which it was derived, use spherical harmonics having low order and degree, using  
 247 smaller grid spacings for the HASDM data archive would not have helped much to im-  
 248 prove the resolution of details.

249 For purpose of comparison, the HASDM grid values were interpolated to the cen-  
 250 ters of the geodesic grid cells used in EXEMPLAR. An example of such a comparison  
 251 is shown in Figure 3, from 26 October, 2003 at 6 h Universal Time (UT). In this exam-  
 252 ple (and others not shown) it is apparent that the EXEMPLAR densities have features  
 253 that do not appear in the HASDM map. On the other hand, comparisons of EXEM-  
 254 PLAR densities with CHAMP and GRACE measurements had indicated that small-scale  
 255 variations in the density variations do exist (Weimer et al., 2020). Reports on complex,  
 256 localized density enhancements had previously been reported on numerous occasions (Schlegel  
 257 et al., 2005; Sutton et al., 2005; Bruinsma et al., 2006; Crowley et al., 2010).

258 It was decided that the best way to compare the results from models having dif-  
 259 ferent resolutions is to calculate the mean density on the surface of a sphere at a given  
 260 altitude. The mean values are obtained by first taking the density value in each grid cell  
 261 and multiplying it by the area of that cell, and then summing these products. In the case

262 of the HASDM database, the interpolated values are used. As the grid areas were pre-  
263 computed in units of square radians, the integrated totals only need to be divided by  $4\pi$   
264 to obtain the mean value in units of  $\text{kg}/\text{m}^3$ . In the example in Figure 3, the means are  
265 indicated above each map in the upper-right corners. These values were computed for  
266 every 3 hr interval in the SET HASDM density database, for the entire 20-year time pe-  
267 riod, at altitudes of 200, 300, 400, 600, and 800 km. The results are shown as a function  
268 of time in Figure 4, with the HASDM values indicated with the black lines and the EX-  
269 TEMPLAR results drawn with the red lines. For comparison, density values from the  
270 NRLMSIS 2.0 model, without the exospheric temperature modifications, are shown with  
271 the blue lines to show whether or not the EXTEMPLAR model yields improvements.  
272 The red lines are more visible as they are drawn last. Solar wind velocity and IMF val-  
273 ues measured by the Advanced Composition Explorer (ACE) spacecraft during this time  
274 period were input to the Poynting flux model used in the EXTEMPLAR program, us-  
275 ing the Level 2 science data.

276 Obviously, the three models are in excellent agreement at most altitudes, although  
277 HASDM often has slightly larger values. The differences are largest at 200 km. While  
278 the models track the same trends over time, the HASDM values at this altitude tend to  
279 be larger than from EXTEMPLAR and NRLMSIS. However, as illustrated in Figure 2,  
280 at 200 km altitude the variations in the exospheric temperature have little influence on  
281 the density at this altitude; the density values at this altitude are determined almost en-  
282 tirely by the conditions calculated within the NRLMSIS 2.0 model. One thing appar-  
283 ent in Figure 4 is that the density changes at 600 to 800 km span a range of over two  
284 decades, while at 200 km the range is only a factor of five. Additional details can be seen  
285 in the Supporting Information document that contains 20 separate plots for each of the  
286 years in the SET HASDM density database. This supplement contains an additional 20  
287 plots with the logarithm of the ratios of the EXTEMPLAR and NRLMSIS densities with  
288 respect to the HASDM densities.

289 A closer look at the time period spanning years 2001 through 2004 is shown in Fig-  
290 ure 5, for altitudes 800, 600, 400, and 300 km, from top to bottom. The periodic geo-  
291 magnetic activity due to the solar rotation and major storms are more visible in this graph.  
292 Departures between the EXTEMPLAR and NRLMSIS results are more apparent.

293 An expanded look at the active time period in late 2003 is presented in Figure 6,  
 294 covering the time period from 16 October through 24 November 2003, containing two  
 295 extreme geomagnetic storms. In this graph it is seen that the EXEMPLAR model (red)  
 296 tracks the HASDM values (black) better than the NRLMSIS values (blue), and matches  
 297 the variations during the major storms very well.

298 Figure 7 contains another interesting time period, from 1 July 2004 through 30 Novem-  
 299 ber 2004. The first event within this interval has three, successive peaks in the neutral  
 300 density, followed by an event in November having two larger density peaks in succession.  
 301 In both events the EXEMPLAR results track the HASDM results very well, particu-  
 302 larly in the rapid decline in the densities after the peaks, although there are time peri-  
 303 ods where the unmodified NRLMSIS model does better in matching the HASDM vari-  
 304 ations.

## 305 5 Correlations, Standard Deviations, and Ratios

306 Linear correlation coefficients of the mean density values were calculated for each  
 307 of the 20 years, with the results shown in Figure 8. The panel in 8(a) shows the corre-  
 308 lations between the EXEMPLAR and HASDM values, while the panel in 8(e) to the  
 309 right shows the NRLMSIS-HASDM correlations. The blue, red, green, brown, and black  
 310 lines represent altitudes of 200, 300, 400, 600, and 800 km, respectively. In general, the  
 311 EXEMPLAR-HASDM correlations range from 0.90 to 0.98 for altitudes of 300 to 600  
 312 km, while the correlation for 200 km altitude tends to range from only 0.82 to 0.94. The  
 313 correlations at 800 km are more variable, being in the high range in some years, but de-  
 314 creasing in years associated with low solar activity (2007–2009 and 2018–2019). The NRLM-  
 315 SIS model has correlations with HASDM that are generally lower, with differences rang-  
 316 ing from about 0.02 to 0.1, and greater differences (worse correlation) at 800 km alti-  
 317 tude.

318 Standard deviations are shown in Figures 8(b) for EXEMPLAR and 8(f) for NRLM-  
 319 SIS, using the same line coloring at each altitude. Dividing these deviations by the mean  
 320 of the HASDM density in each year results in the deviation expressed as a percentage,  
 321 shown in panels 8(c) and 8(g). With the exception of the deviations at 800 km altitude  
 322 before 2005, these percentage errors mostly fall in the range of 10% to 20% for EXTEM-  
 323 PLAR. The standard deviations for NRLMSIS are approximately the same at altitudes

324 of 200 to 400 km, except much higher (worse) at 400 km during the times of low solar  
 325 activity. At 600 and 800 km altitudes the NRLMSIS standard deviations tend to be al-  
 326 ways greater than the EXTEMLAR values.

327 The bottom row in Figure 8 shows the ratios between the model densities as a func-  
 328 tion of time. 8(d) shows the base 10 logarithm of EXTEMLAR/HASDM density ra-  
 329 tios and 8(h) to the right shows the same for NRLMSIS/HASDM ratios. Ideally, the ra-  
 330 tio should be one, with a logarithm of zero. Most of the time the logarithm of the EX-  
 331 TEMPLAR ratios in 8(d) are in the range of about -0.1 to -0.05 (indicating densities slightly  
 332 less than the HASDM values by a factor of .79 to .89), with better results at 600 and  
 333 800 km in the years 2006, 2007, and 2019. The NRLMSIS ratios had greater variabil-  
 334 ity over time and at different altitudes, ranging from negative to positive ratios, partic-  
 335 ularly during the years of low solar activity (2007–2009 and 2018–2019).

336 For comparison with our results, Figure 9 contains estimates of the HASDM er-  
 337 rors, that were produced by B. Bowman and provided by Tobiska et al. (2021) in a sup-  
 338 plement at <https://spacewx.com/hasdm/>. These errors are derived within HASDM by  
 339 a process known as the Dynamic Calibration Atmosphere (DCA) (Storz et al., 2005).  
 340 The dots in Figure 8 show the HASDM error as a percentage, for each of the calibra-  
 341 tion satellites. The HASDM errors tend to range between 2% and 6% during the peaks  
 342 in the solar cycle (e.g., Figures 8(a) and 8(c)) and increasing to 4% to 10% when solar  
 343 activity is low (e.g., Figures 8(b) and 8(d)). These uncertainties were obtained by com-  
 344 paring the derived HASDM data assimilated densities with sets of densities derived from  
 345 segmented tracking orbit fits to calibration satellites. It is seen in these graphs that the  
 346 errors are largest at 750 km altitude and above.

## 347 6 Discussion

348 The method in which the neutral densities from different models were integrated  
 349 over the surface of a sphere at a given altitude has proven to be an effective way to make  
 350 comparisons. The results show a very good agreement between the EXTEMLAR and  
 351 HASDM models on scales ranging from years down to hours. The correlations between  
 352 the two models at the smallest scales, as seen in Figures 6 and 7 are excellent. The EX-  
 353 TEMPLAR predictions match the HASDM values especially well during the most ex-  
 354 treme events, most notably at 400 km altitude and above. In general, the EXTEMLAR

355 method improved upon the unmodified density predictions from the NRLMSIS model,  
356 resulting in higher correlations, lower standard deviations, and more consistent ratios  
357 in comparison with the HASDM densities. However, there are times when the NRLM-  
358 SIS model is in better agreement with the HASDM values.

359 The results shown here are helpful for illustrating how the thermosphere behaves  
360 over time at different altitudes, including the annual and solar cycle variability in ad-  
361 dition to during major events. It is seen that geomagnetic storms have the greatest in-  
362 fluence at higher altitudes, where there are substantial changes in the neutral density  
363 with respect to pre-storm levels.

364 The correlations graphed in Figure 8(a) for the EXTEMLAR-HASDM densities  
365 at altitudes of 300–600 km are approximately 0.95, which we consider to be very good.  
366 While the correlations at 200 km altitude are lower (in the range of 0.82 to 0.94), they  
367 are still reasonable. At 200 km altitude the exospheric temperature calculations have lit-  
368 tle effect on the density variations, as shown in Figure 2.

369 Results at 800 km are the most inconsistent. Figure 9 also indicates that the HASDM  
370 errors are the largest here, particularly during times of low solar activity, as shown in  
371 9(b) and 9(d). Solar minimum also coincides with the lowest correlations at 800 km (black  
372 line in Figure 8). The plots in the Supporting Information for the years 2007–2009, and  
373 2017–2019 show that the densities from the HASDM system have a relatively flat line  
374 at this altitude, while the NRLMSIS model produced variations in the density that are  
375 the expected signatures of the semi-annual oscillations (J. T. Emmert & Picone, 2010).  
376 As the EXTEMLAR method uses NRLMSIS to calculate densities, it also has the semi-  
377 annual oscillations. The most likely explanation for the flat response in the HASDM sys-  
378 tem is that the model it is based on lacks sufficient variation in the amount of atomic  
379 oxygen and or helium.

380 At 800 km altitude the EXTEMLAR densities tend to exceed the HASDM val-  
381 ues during the large geomagnetic storms, such as in late October in Figure 6(a). This  
382 is the cause of the increase in the black line in 2003 in Figure 8(c). It can be argued that  
383 the densities calculated by the EXTEMLAR-MSIS combination could more accurate  
384 than HASDM at this altitude, since the sparse atmosphere may have little effect on the  
385 segmented orbit density fits.

386 It was mentioned earlier that HASDM has a coarse spatial resolution, while satel-  
387 lite measurements indicate that the density often varies over distances that are smaller  
388 than can be resolved with this model. In cases where the total densities of the two mod-  
389 els are in agreement, the EXEMPLAR-MSIS combination is likely more accurate.

390 Oftentimes the integrated densities from HASDM are slightly greater than those  
391 from EXEMPLAR. In a comparison between the SET HASDM dataset with the JB2008  
392 model and CHAMP and GRACE density measurements, Licata et al. (2021) had found  
393 that the HASDM density values were also consistently greater than the values derived  
394 from the CHAMP and GRACE accelerometer measurements, while matching better than  
395 the JB2008 model. Licata et al. (2021) also found that during the major storm in Oc-  
396 tober 2003 (the same event shown here in the first half of Figure 6), while the HASDM  
397 dataset had slightly larger densities than measured with CHAMP and GRACE, it did  
398 very well at matching the relative changes in density during this period.

399 It would be possible to modify the NRLMSIS model to bring it (and EXEMPLAR)  
400 in better agreement with the HASDM densities. For example, changes could be made  
401 in composition and derivatives at the lower boundary of the thermosphere. On the other  
402 hand the density values from HASDM may have a bias, so first it would be necessary  
403 to resolve the reasons for why the HASDM and NRLMSIS models differ at some alti-  
404 tudes before committing to any modifications. As reported by J. Emmert (2015), the  
405 estimation of coefficients of drag and ballistic coefficients “is quite challenging even for  
406 objects whose mass, geometry, and composition are precisely known.”

## 407 **7 Conclusion**

408 The comparison of the densities calculated by the EXEMPLAR program with the  
409 values in the SET HASDM density database show that EXEMPLAR performs very  
410 well. As the HASDM assimilation system relies on radar tracking of multiple satellites  
411 to derive the neutral densities, it is expected to be very accurate. But it cannot predict  
412 the response of the neutral density to sudden geomagnetic storms in advance, before the  
413 tracking measurements can be obtained. On the other hand, the EXEMPLAR program  
414 can use the real-time measurements of the solar wind velocity and IMF to make predic-  
415 tions approximately 1 hr ahead of the thermosphere’s response to extreme space weather

416 events. This lead provides time to issue alerts or calculate perturbations to satellite or-  
 417 bits.

418 The EXEMPLAR results shown here had used Level 2 science data from the ACE  
 419 satellite, which had a better quality than the real-time data provided by ACE. Presently  
 420 the real-time solar wind measurements are provided by the Deep Space Climate Obser-  
 421 vatory (DSCOVR). The quality of the real-time DSCOVR solar wind and magnetic field  
 422 measurements are just as good as the ACE Level 2 data, so this change will not degrade  
 423 the performance of EXEMPLAR. The solar indices are also updated in near real time  
 424 by SET.

425 Other developers of thermosphere models, either empirical or numerical, are en-  
 426 couraged to compare their neutral density calculations with the SET HASDM density  
 427 database in a similar manner. The total, integrated densities shown in Figure 4 are avail-  
 428 able in an archive at <https://doi.org/10.5281/zenodo.5177065> for the entire, 20 year  
 429 time period. As mentioned earlier, these data are of value for studying how the neutral  
 430 density at different altitudes vary on time scales ranging from hours to solar cycles.

## 431 Acronyms

432 **ACE** Advanced Composition Explorer

433 **CHAMP** Challenging Mini-satellite Payload satellite

434 **DCA** Dynamic Calibration Atmosphere

435 **DSCOVR** Deep Space Climate Observatory

436 **EXEMPLAR** EXospheric TEMperatures on a PoLyhedrAl gRid

437 **GRACE** Gravity Recovery and Climate Experiment satellite

438 **HASDM** High Accuracy Satellite Drag Model

439 **JB2008** Jacchia-Bowman 2008 neutral density model

440 **MSIS** Short abbreviation referring to the either of the NRL density models

441 **NRLMSISE-00** Naval Research Laboratory Mass Spectrometer and Incoherent Scat-  
 442 ter radar Extended density model 2000

443 **NRLMSIS 2.0** Naval Research Laboratory Mass Spectrometer and Incoherent Scat-  
 444 ter radar model, Version 2.0

445 **SET** Space Environment Technologies

## Data Availability Statement

A data archive containing the integrated neutral densities on spherical shells at altitudes of 200, 300, 400, 600, and 800 km, from both EXEMPLAR and HASDM, is available at <https://doi.org/10.5281/zenodo.5177065>. The Supporting Information document contains graphs of these integrated densities for each of the 20 years. The original SET-HASDM database access and supplementary information can be found at <https://spacewx.com/hasdm/>. The ACE level 2 data are available from the NASA archives at <https://cdaweb.gsfc.nasa.gov/pub/data/ace>. The solar indices are available at <https://spacewx.com/jb2008/>.

(The reserved Zenodo DOI link noted above will become active only after this paper is accepted. A temporary copy of this archive is now at: <https://bit.ly/2X79AZ4>)

## Acknowledgments

Daniel Weimer was supported by NASA grant 80NSSC20K1362 to Virginia Tech, through the Space Weather Operations-to-Research Program. Kent Tobiska, Piyush Mehta, and Richard Licata were supported by subcontracts to Space Environment Technologies and West Virginia University. Kent Tobiska and J. Yoshii also acknowledge support from the DARPA/Leidos AtmoSense contracts HR001121C0081/P0102500070 to Space Environment Technologies. Douglas Drob was supported by NASA interagency agreement 80HQTR20T0081 with the Naval Research Laboratory. Daniel Weimer had additional support from NSF grant AGS-2019465.

## References

- Astafyeva, E., Zakharenkova, I., Huba, J. D., Doornbos, E., & van den IJssel, J. (2017). Global ionospheric and thermospheric effects of the June 2015 geomagnetic disturbances: Multi-instrumental observations and modeling. *J. Geophys. Res.: Space Physics*, *112*, 11,716–11,742. doi: 10.1002/2017JA024174
- Bowman, B. R., Tobiska, W. K., Marcos, F. A., Huang, C. Y., Lin, C. S., & Burke, W. J. (2008). A new empirical thermospheric density model JB2008 using new solar and geomagnetic indices. In *AIAA/AAS astrodynamics specialist conference proceedings*. Honolulu, HI.

- 476 Bruisma, S., Forbes, J. M., Nerem, R. S., & Zhang, X. (2006). Thermosphere  
 477 density response to the 20–21 November 2003 solar and geomagnetic storm  
 478 from CHAMP and GRACE accelerometer data. *J. Geophys. Res.*, *111*. doi:  
 479 10.1029/2005JA011284
- 480 Bruisma, S., Sutton, E., Solomon, S. C., Fuller-Rowell, T., & Fedrizzi, M. (2018).  
 481 Space weather modeling capabilities assessment: Neutral density for orbit  
 482 determination at low earth orbit. *Space Weather*, *16*(11), 1806–1816. doi:  
 483 10.1029/2018SW002027
- 484 Bruisma, S., Tamagnan, D., & Biancale, R. (2004). Atmospheric densities derived  
 485 from CHAMP/STAR accelerometer observations. *Planet. Space Sci.*, *52*, 297.
- 486 Case, N. A., & Wild, J. A. (2012). A statistical comparison of solar wind prop-  
 487 agation delays derived from multispacecraft techniques. *Journal of Geo-*  
 488 *physical Research: Space Physics*, *117*(A2). Retrieved from [https://](https://agupubs.onlinelibrary.wiley.com/doi/abs/10.1029/2011JA016946)  
 489 [agupubs.onlinelibrary.wiley.com/doi/abs/10.1029/2011JA016946](https://agupubs.onlinelibrary.wiley.com/doi/abs/10.1029/2011JA016946) doi:  
 490 <https://doi.org/10.1029/2011JA016946>
- 491 Crowley, G., Knipp, D. J., Drake, K. A., Lei, J., Sutton, E., & Lühr, H. (2010).  
 492 Thermospheric density enhancements in the dayside cusp region during strong  
 493  $B_Y$  conditions. *Geophys. Res. Lett.*, *37*. doi: 10.1029/2009GL042143
- 494 Emmert, J. (2015). Thermospheric mass density: A review. *Advances in Space*  
 495 *Research*, *56*(5), 773 - 824. Retrieved from [http://www.sciencedirect.com/](http://www.sciencedirect.com/science/article/pii/S0273117715003944)  
 496 [science/article/pii/S0273117715003944](http://www.sciencedirect.com/science/article/pii/S0273117715003944) doi: <http://dx.doi.org/10.1016/j>  
 497 [.asr.2015.05.038](http://dx.doi.org/10.1016/j.asr.2015.05.038)
- 498 Emmert, J. T., Drob, D. P., Picone, J. M., Siskind, D. E., Jones Jr, M., Mlynczak,  
 499 M. G., ... Yuan, T. (2020). NRLMSIS 2.0: A whole-atmosphere empirical  
 500 model of temperature and neutral species densities. *Earth and Space Science*,  
 501 *7*, e2020EA001321. Retrieved from [https://agupubs.onlinelibrary.wiley](https://agupubs.onlinelibrary.wiley.com/doi/abs/10.1029/2020EA001321)  
 502 [.com/doi/abs/10.1029/2020EA001321](https://agupubs.onlinelibrary.wiley.com/doi/abs/10.1029/2020EA001321) doi: 10.1029/2020EA001321
- 503 Emmert, J. T., & Picone, J. M. (2010). Climatology of globally averaged ther-  
 504 mospheric mass density. *J. Geophys. Res.*, *115*(A09326). doi: 10.1029/  
 505 2010JA015298
- 506 Friis-Christensen, E., Lühr, H., & Hulot, G. (2006). Swarm: A constellation to study  
 507 the Earth's magnetic field. *Earth, Planets and Space*, *58*(4), 351–358. doi: 10  
 508 .1186/BF03351933

- 509 Hedin, A. E. (1991). Extension of the MSIS thermosphere model into the middle  
510 and lower atmosphere. *J. Geophys. Res.*, *96*, 1159–1172.
- 511 Licata, R. J., Mehta, P. M., Tobiska, W. K., Bowman, B. R., & Pilinski, M. D.  
512 (2021). Qualitative and quantitative assessment of the SET HASDM database.  
513 *Space Weather*, *n/a(n/a)*, e2021SW002798. Retrieved from [https://](https://agupubs.onlinelibrary.wiley.com/doi/abs/10.1029/2021SW002798)  
514 [agupubs.onlinelibrary.wiley.com/doi/abs/10.1029/2021SW002798](https://agupubs.onlinelibrary.wiley.com/doi/abs/10.1029/2021SW002798) doi:  
515 <https://doi.org/10.1029/2021SW002798>
- 516 Mehta, P. M., Walker, A. C., Sutton, E. K., & Godinez, H. C. (2017). New  
517 density estimates derived using accelerometers on board the CHAMP and  
518 GRACE satellites. *Space Weather*, *15*(4), 558–576. (2016SW001562) doi:  
519 [10.1002/2016SW001562](https://doi.org/10.1002/2016SW001562)
- 520 Picone, J., Hedin, A., Drob, D., & Aikin, A. (2002). NRLMSISE-00 empirical model  
521 of the atmosphere: Statistical comparisons and scientific issues. *J. Geophys.*  
522 *Res.*, *107*(A12). doi: [10.1029/2002JA009430](https://doi.org/10.1029/2002JA009430)
- 523 Prölss, G. W., & Bird, M. K. (2004). *Physics of the earth's space environment: An*  
524 *introduction*. Springer-Verlag Berlin Heidelberg. (ISBN 3-540-21426-7)
- 525 Reigber, C. H., Lühr, H., & Schwintzer, P. (2002). CHAMP mission status. *Ad-*  
526 *vances in Space Research*, *30*(2), 129–134. doi: [10.1016/S0273-1177\(02\)00276](https://doi.org/10.1016/S0273-1177(02)00276-4)  
527 *-4*
- 528 Schlegel, K., Lühr, H., St.-Maurice, J.-P., Crowley, G., & Hackert, C. (2005). Ther-  
529 mospheric density structures over the polar regions observed with CHAMP.  
530 *Ann. Geophys.*, *23*, 1659–1672.
- 531 Storz, M. F., Bowman, B. R., Branson, M. J. I., J.Casali, S., & Tobiska, W. K.  
532 (2005). High accuracy satellite drag model (HASDM). *Advances in Space*  
533 *Research*, *36*(12), 2497–2505. doi: <https://doi.org/10.1016/j.asr.2004.02.020>
- 534 Sutton, E. K. (2008). *Effects of solar disturbances on the thermosphere densities and*  
535 *winds from CHAMP and GRACE satellite accelerometer data* (Unpublished  
536 doctoral dissertation). University of Colorado, Boulder.
- 537 Sutton, E. K., Forbes, J. M., & Nerem, R. S. (2005). Global thermospheric  
538 neutral density and wind response to the severe 2003 geomagnetic storms  
539 from CHAMP accelerometer data. *J. Geophys. Res.*, *110*. doi: [10.1029/](https://doi.org/10.1029/2004JA010985)  
540 [2004JA010985](https://doi.org/10.1029/2004JA010985)
- 541 Tapley, B. D., Watkins, S. B. M., & Reigber, C. (2004). The gravity recovery and

- 542 climate experiment: Mission overview and early results. *Geophys. Res. Lett.*,  
 543 *31*. doi: 10.1029/2004GL019929
- 544 Thayer, J. P., Tobiska, W. K., Pilinski, M. D., & Sutton, E. K. (2021). Remaining  
 545 issues in upper atmosphere satellite drag. In *Space weather effects and ap-*  
 546 *plications* (pp. 111–140). American Geophysical Union (AGU). Retrieved  
 547 from [https://agupubs.onlinelibrary.wiley.com/doi/abs/10.1002/](https://agupubs.onlinelibrary.wiley.com/doi/abs/10.1002/9781119815570.ch5)  
 548 [9781119815570.ch5](https://doi.org/10.1002/9781119815570.ch5) doi: <https://doi.org/10.1002/9781119815570.ch5>
- 549 Tobiska, W. K., Bouwer, S. D., & Bowman, B. R. (2008). The development of new  
 550 solar indices for use in thermospheric density modeling. *J. Atmos. Sol. Terr.*  
 551 *Phys.*, *70*, 803–819.
- 552 Tobiska, W. K., Bowman, B. R., Bouwer, S. D., Cruz, A., Wahl, K., Pilinski,  
 553 M. D., ... Licata, R. J. (2021). The SET HASDM density database.  
 554 *Space Weather*, *19*(4), e2020SW002682. Retrieved from [https://](https://agupubs.onlinelibrary.wiley.com/doi/abs/10.1029/2020SW002682)  
 555 [agupubs.onlinelibrary.wiley.com/doi/abs/10.1029/2020SW002682](https://doi.org/10.1029/2020SW002682) doi:  
 556 <https://doi.org/10.1029/2020SW002682>
- 557 van den IJssel, J., Doornbos, E., Iorfida, E., March, G., Siemes, C., & Montenbruck,  
 558 O. (2020). Thermosphere densities derived from Swarm GPS observations.  
 559 *Advances in Space Research*, *65*(7), 1758–1771. Retrieved from [https://](https://www.sciencedirect.com/science/article/pii/S0273117720300077)  
 560 [www.sciencedirect.com/science/article/pii/S0273117720300077](https://doi.org/10.1016/j.asr.2020.01.004) doi:  
 561 <https://doi.org/10.1016/j.asr.2020.01.004>
- 562 Weimer, D. R. (2005a). Improved ionospheric electrodynamic models and applica-  
 563 tion to calculating Joule heating rates. *J. Geophys. Res.*, *110*. doi: 10.1029/  
 564 2004JA010884
- 565 Weimer, D. R. (2005b). Predicting surface geomagnetic variations using ionospheric  
 566 electrodynamic models. *J. Geophys. Res.*, *110*. doi: 10.1029/2005JA011270
- 567 Weimer, D. R., Mehta, P. M., Tobiska, W. K., Doornbos, E., Mlynczak, M. G.,  
 568 Drob, D. P., & Emmert, J. T. (2020). Improving neutral density predictions  
 569 using exospheric temperatures calculated on a geodesic, polyhedral grid. *Space*  
 570 *Weather*, *18*(1), e2019SW002355. doi: 10.1029/2019SW002355
- 571 Weimer, D. R., Mlynczak, M. G., Emmert, J. T., Doornbos, E., Sutton, E. K., &  
 572 Hunt, L. A. (2018). Correlations between the thermosphere’s semiannual den-  
 573 sity variations and infrared emissions measured with the SABER instrument.  
 574 *J. Geophys. Res. Space Physics*, *123*. doi: 10.1029/2018JA025668

575 Weimer, D. R., Sutton, E. K., Mlynczak, M. G., & Hunt, L. A. (2016). Intercalibra-  
576 tion of neutral density measurements for mapping the thermosphere. *J. Geo-*  
577 *phys. Res.*, *121*, 5975–5990. doi: 10.1002/2016JA022691

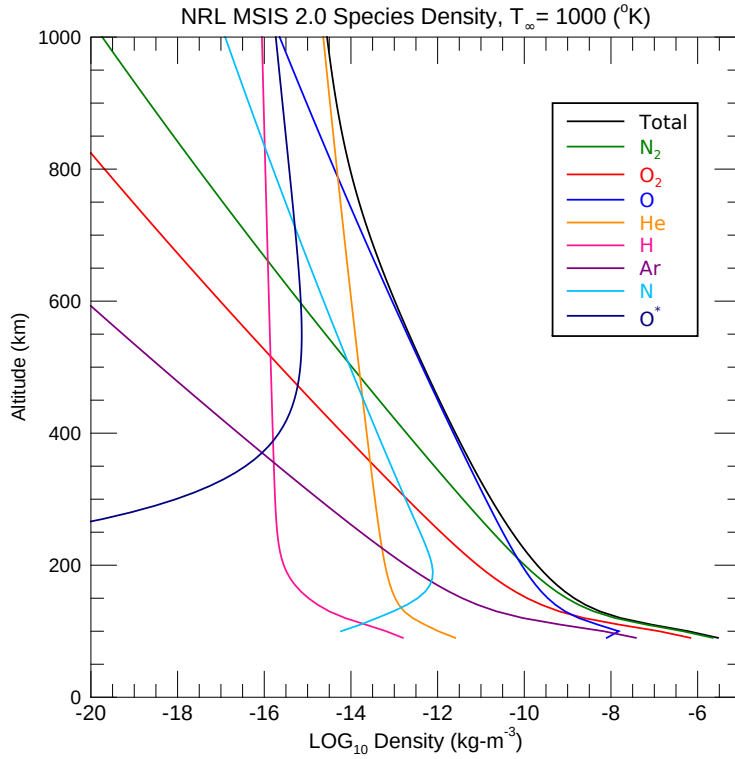


**Figure 1.** Example of densities from NRLMSIS 2.0 as a function of altitude. All species that are calculated are shown, using colors indicated in the legend. Total density shown in black. Input values were  $80^{\circ}$  latitude, 0 longitude, on Spring equinox at 0 Universal Time.  $F_{10.7}$  index was 120 sfu, and  $A_p$  index zero, with exospheric temperature set to  $1000^{\circ}\text{K}$ .

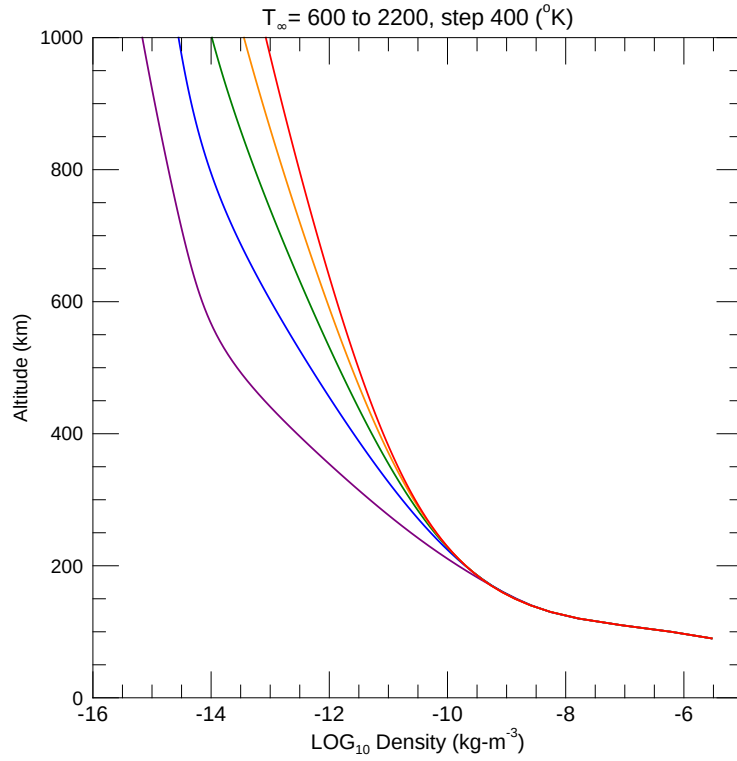


**Figure 2.** Example of total densities from NRLMSIS 2.0 as a function of altitude, for different values of exospheric temperature. The five lines show results with the exospheric temperature set to 600°, 1000°, 1400°, 1800°, and 2200°K, using the colors purple, blue, green, orange, and red, respectively. Other input parameters are the same as in Figure 1.

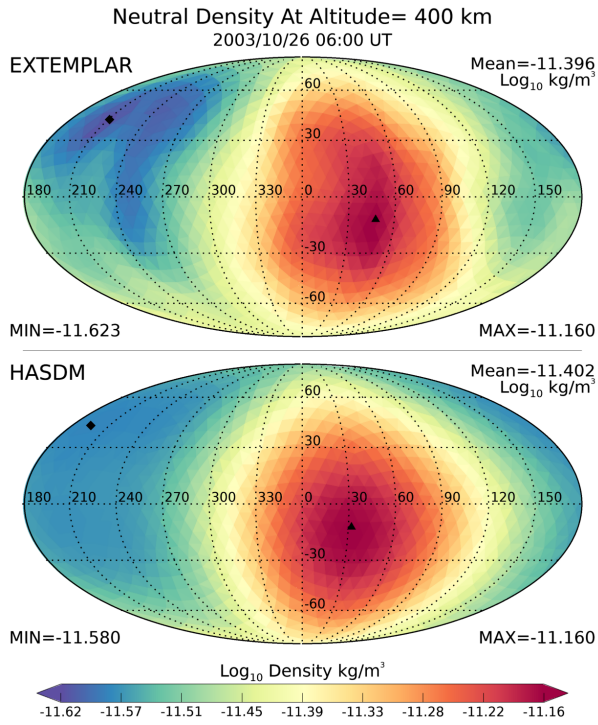


**Figure 3.** Example of neutral densities from EXTEMLAR (top) and HASDM (bottom), mapped at 400 km altitude. Values are calculated for 26 October, 2003, at 6 h UT. The values in the upper right corners show the mean values of the densities at this altitude, with minimum and maximum values indicated in the lower left and right corners. All units are the base 10 logarithm of the density in kg/m<sup>3</sup>.

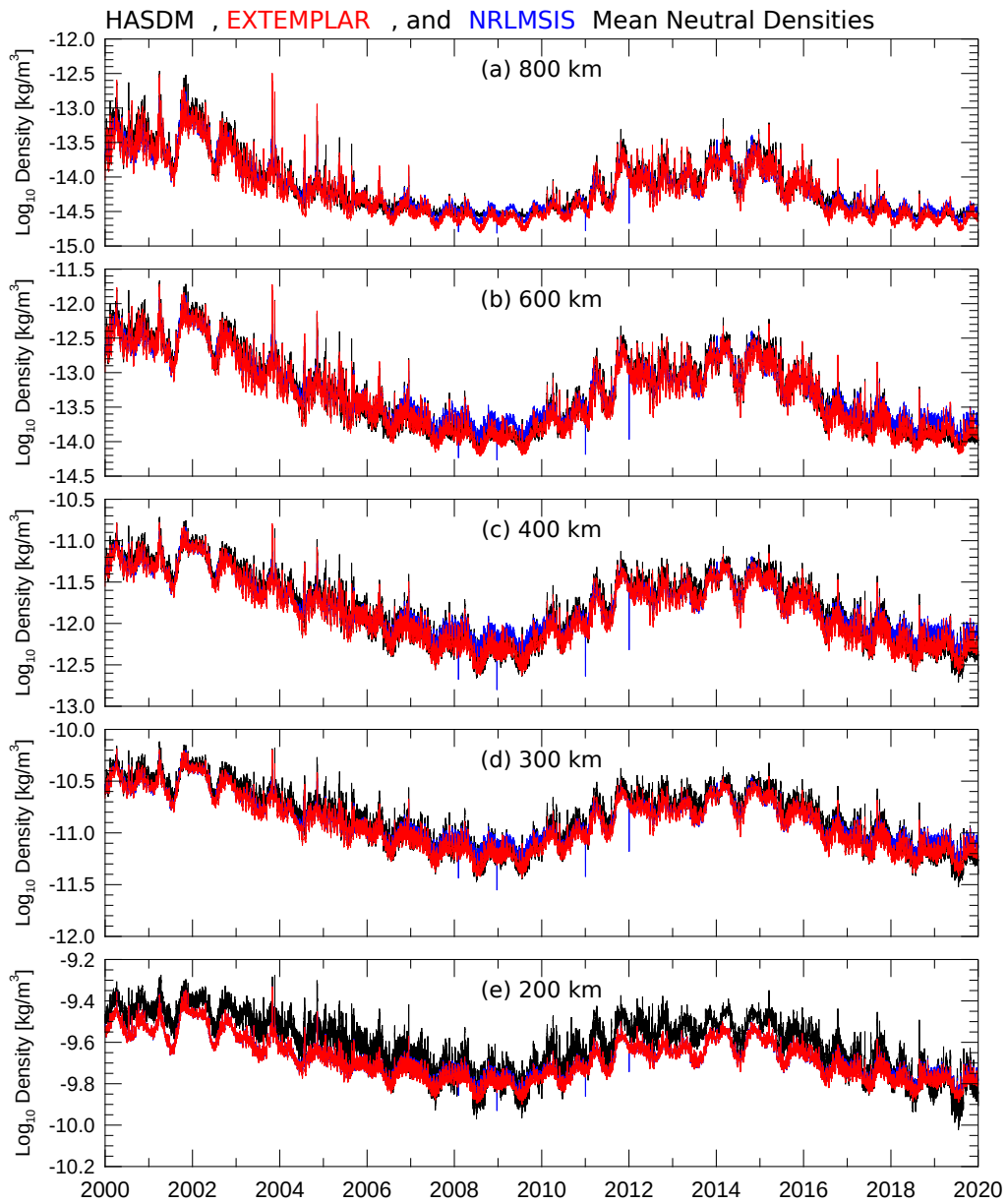


**Figure 4.** Mean values of densities graphed as a function of time, using a logarithmic scale, for the time period from 1 January, 2000 through 31 December, 2019. HASDM results are shown in black, EXEMPLAR in red, and NRLMSIS 2.0 values in blue, for altitudes of 800, 600, 400, 300, and 200 km (top to bottom).

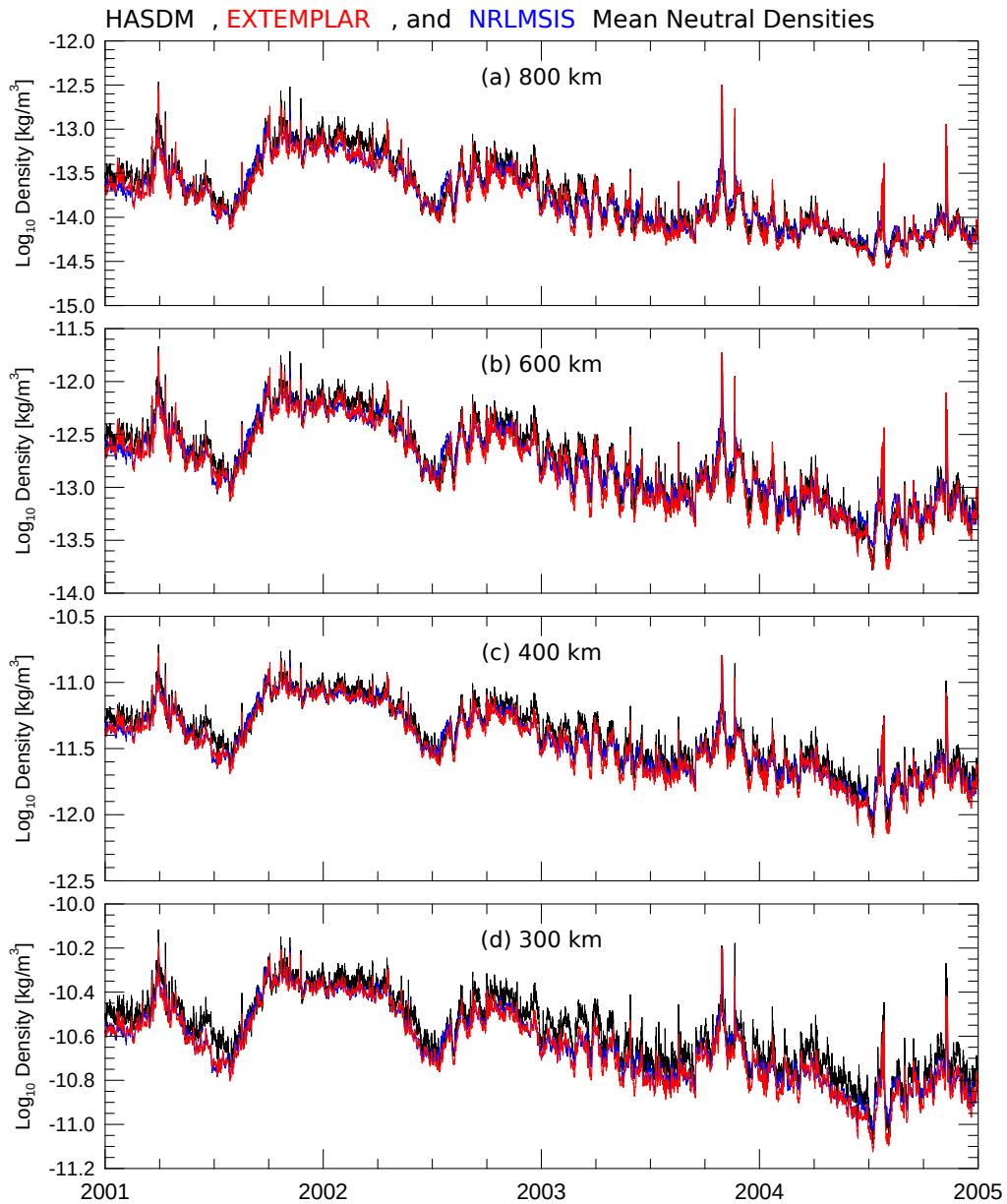


**Figure 5.** Mean values of densities graphed as a function of time, using a logarithmic scale, for the time period from 1 January, 2001 through 31 December, 2004. HASDM results are shown in black, EXEMPLAR in red, and NRLMSIS 2.0 values in blue, for altitudes of 800, 600, 400, and 300 km (top to bottom).

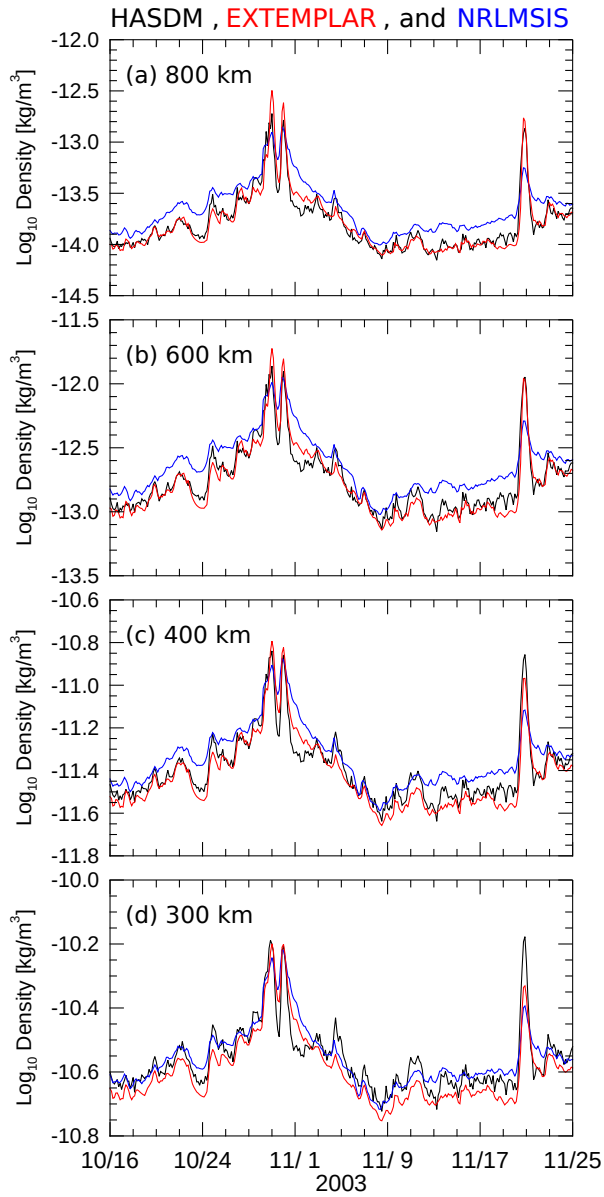


**Figure 6.** Mean values of densities graphed as a function of time, using a logarithmic scale, for the time period from 16 October through 24 November 2003. HASDM results are shown in black, EXEMPLAR in red, and NRLMSIS 2.0 values in blue, for altitudes of 800, 600, 400, and 300 km (top to bottom).

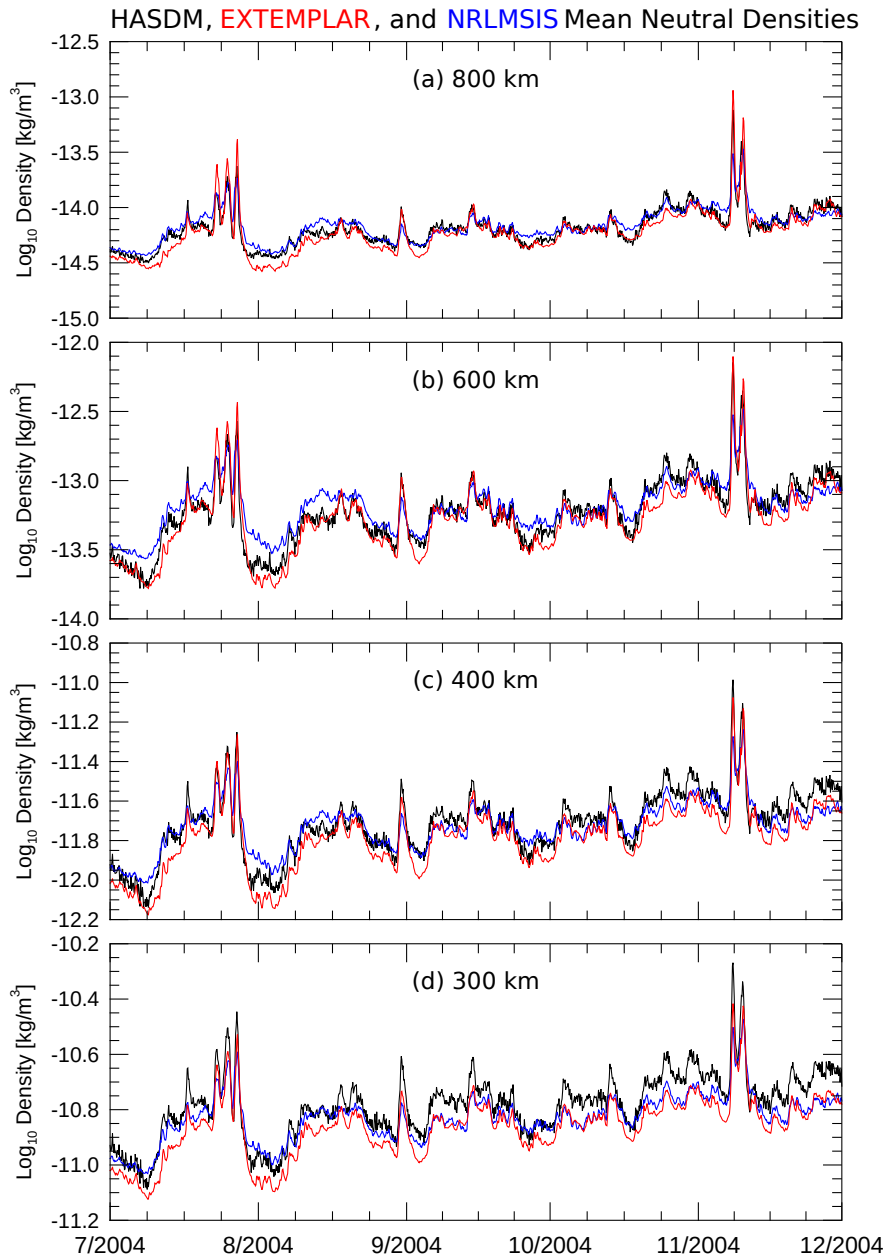


**Figure 7.** Mean values of densities graphed as a function of time, using a logarithmic scale, for the time period from 1 July 2004 through 30 November 2004. HASDM results are shown in black, EXTEMLAR in red, and NRLMSIS 2.0 values in blue, for altitudes of 800, 600, 400, and 300 km (top to bottom).

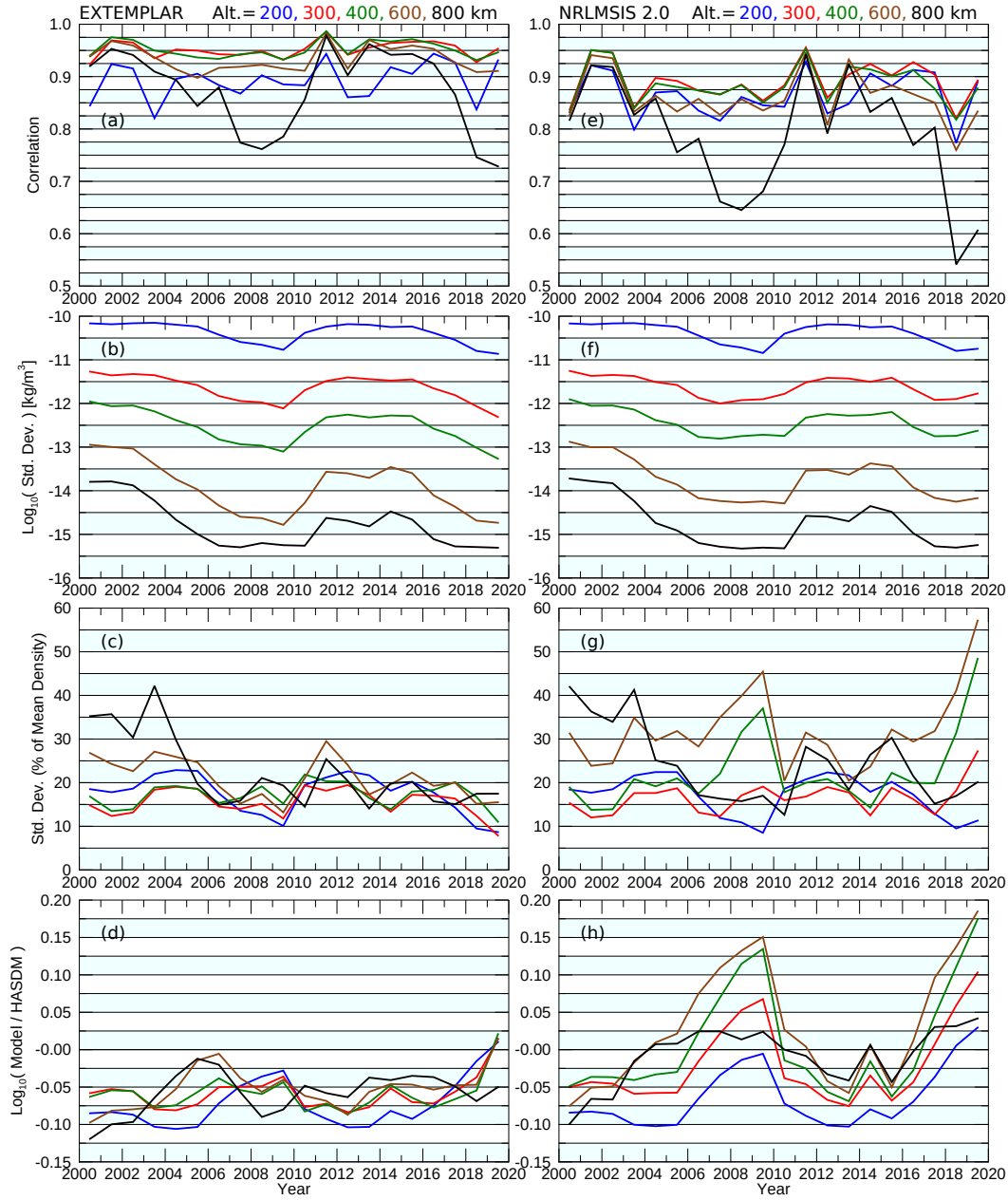


**Figure 8.** Model correlations, standard deviations, and ratios. EXTEMLAR results are in the left column and NRLMSIS 2.0 results are in the right column. (a) and (e) Coefficients of correlation for all years. The blue, red, green, brown, and black lines represent altitudes of 200, 300, 400, 600, and 800 km, respectively. (b) and (f) Standard deviations, in units of  $\text{kg/m}^3$ , using the same line colors. (c) and (g) Standard deviations expressed as a percentage of the HASDM mean density in each year. (d) and (h) Base 10 logarithm of the ratio between the model and HASDM density, showing the mean value in each year.

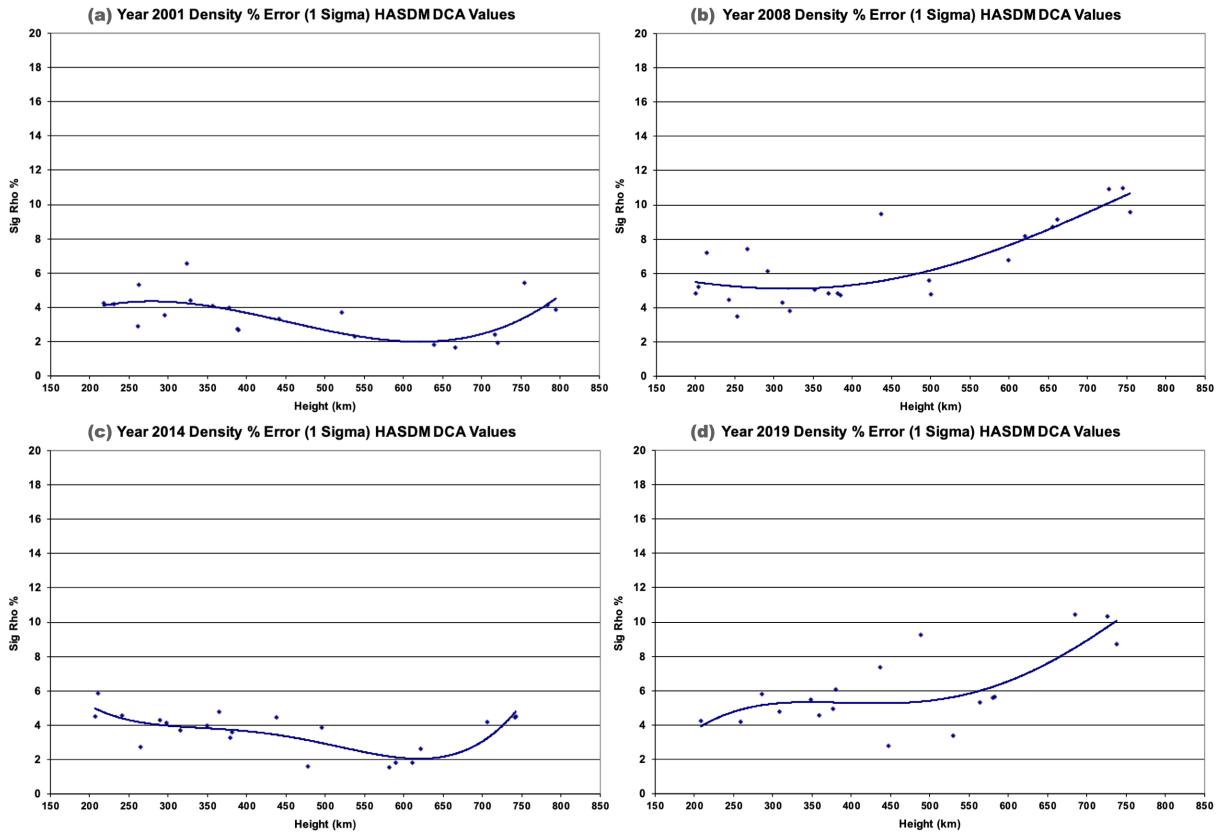


**Figure 9.** HASDM errors as a function of altitude. The four parts show the errors for the years (a) 2001, (b) 2008, (c) 2014, and (d) 2019.